JMEPEG (2012) 21:2207–2217
DOI: 10.1007/s11665-011-0118-7

1059-9495/$19.00

# Modifications in the AA5083 Johnson-Cook Material Model for Use in Friction Stir Welding Computational Analyses

*M. Grujicic, B. Pandurangan, C.-F. Yen, and B.A. Cheeseman*

*(Submitted December 2, 2011)*

**Johnson-Cook strength material model is frequently used in finite-element analyses of various manufacturing processes involving plastic deformation of metallic materials. The main attraction to this model arises from its mathematical simplicity and its ability to capture the first-order metal-working effects (e.g., those associated with the influence of plastic deformation, rate of deformation, and the attendant temperature). However, this model displays serious shortcomings when used in the engineering analyses of various hot-working processes (i.e., those utilizing temperatures higher than the material recrystallization temperature). These shortcomings are related to the fact that microstructural changes involving: (i) irreversible decrease in the dislocation density due to the operation of annealing/recrystallization processes; (ii) increase in grain-size due to high-temperature exposure; and (iii) dynamic-recrystallization-induced grain refinement are not accounted for by the model. In this study, an attempt is made to combine the basic physical-metallurgy principles with the associated kinetics relations to properly modify the Johnson-Cook material model, so that the model can be used in the analyses of metal hot-working and joining processes. The model is next used to help establish relationships between process parameters, material microstructure and properties in friction stir welding welds of AA5083 (a non-age-hardenable, solid-solution strengthened, strain-hardened/stabilized Al-Mg-Mn alloy).**

**Keywords** AA5083, friction stir welding, Johnson-Cook material model

## 1. Introduction

In this study, an attempt is made to modify the conventional Johnson-cook material-strength model often used in the engineering analyses of various metal-working processes. The modified Johnson-Cook material model is then used in a transient non-linear dynamics finite-element analysis of a butt friction stir welding (FSW) process of AA5083-H131 (a non-age-hardenable, solid-solution strengthened, strain-hardened/stabilized Al-Mg-Mn alloy). Hence, the main topics covered in this study include: (a) Johnson-Cook material model; (b) AA5083-H131; and (c) FSW. These topics are briefly reviewed in the remainder of this section.

### 1.1 Johnson-Cook Material-Strength Model (Ref 1)

Within this model, the subject metallic material is considered as an isotropic linear-elastic and a strain-rate sensitive, strain-hardenable, and (reversibly) thermally softenable plastic material. The purely elastic response of the material is defined using the generalized Hooke's law. On the other hand, the elastic/plastic response of the material is described using the following three relations: (a) a *yield criterion*, i.e., a mathematical relation which defines the condition which must be satisfied for the onset (and continuation) of plastic deformation; (b) a *flow-rule*, i.e., a relation which describes the rate of change of different plastic strain components during plastic deformation; and (c) a *constitutive law*, i.e., a relation which describes how the material-strength changes as a function of the extent of plastic deformation, the rate of deformation and temperature.

For most metallic alloy grades joined using FSW, plasticity is considered to be of a purely distortional (non-volumetric) character and the yield criterion and the flow-rule are, respectively, defined using the vonMises yield criterion and a normality flow-rule. The von Misses yield criterion states that equivalent stress (a scalar, frame-invariant function of stress components) must be equal to the material yield strength for plastic deformation to occur/proceed. The normality flow-rule states that the plastic flow takes place in the direction of the stress-gradient of the yield surface (a locus of the stress/strain points within the associated multidimensional space at which the vonMises stress criterion is satisfied). The Johnson-Cook strength constitutive law is defined as:

$$\sigma_y = A\left[1 + \frac{B}{A}\left(\bar{\varepsilon}^{\mathrm{pl}}\right)^n\right]\left[1 + C\log\left(\dot{\bar{\varepsilon}}^{\mathrm{pl}}\Big/\dot{\bar{\varepsilon}}_0^{\mathrm{pl}}\right)\right]\left[1 - T_H^m\right] \quad \text{(Eq 1)}$$

where $\bar{\varepsilon}^{\mathrm{pl}}$ is the equivalent plastic strain, $\dot{\bar{\varepsilon}}^{\mathrm{pl}}$ the equivalent plastic strain rate, $\dot{\bar{\varepsilon}}_0^{\mathrm{pl}}$ a reference equivalent plastic strain rate, $A$ the zero-plastic-strain, unit-plastic-strain-rate, room-temperature

**M. Grujicic** and **B. Pandurangan**, Department of Mechanical Engineering, Clemson University, 241 Engineering Innovation Building, Clemson, SC 29634-0921; and **C.-F. Yen** and **B.A. Cheeseman**, Army Research Laboratory—Survivability Materials Branch, Aberdeen, Proving Ground, MD 21005-5069. Contact e-mails: mica.grujicic@ces.clemson.edu and gmica@clemson.edu.

yield strength, $B$ the strain-hardening constant, $n$ the strain-hardening exponent, $C$ the strain-rate constant, $m$ the thermal-softening exponent, and $T_H = (T - T_{\text{room}})/(T_{\text{melt}} - T_{\text{room}})$ a room-temperature ($T_{\text{room}}$)-based homologous temperature, while $T_{\text{melt}}$ is the melting temperature. All temperatures are given in Kelvin.

In Eq 1, the parameter $A$ defines the as-annealed material yield strength, the term within the first pair of brackets defines the effect of strain-hardening, the term within the second pair of brackets quantifies the effect of deformation rate, while the last term shows the reversible effect of temperature.

It should be noted that for a given alloy grade, the parameter $A$, depends on the material grain-size. When plastic deformation takes place at a temperature lower than the material recrystallization temperature, the material grain-size (as represented by the grain volume can be considered as being constant). Consequently, parameter $A$ would remain constant, as postulated by the Johnson-Cook material-strength model. However, at elevated temperatures (and in the presence of plastic deformation), one must take into account the effect of grain-coarsening and recrystallization-induced grain-size refinement. Under these conditions, the assumption regarding constancy of parameter $A$ becomes questionable.

Also, the equivalent plastic strain used in the strain-hardening term is a measure of the dislocation density within the material. One could expect that, in the absence of annealing/recrystallization processes that, the equivalent plastic strain and the dislocation density are correlated. However, this condition is not generally met during hot-working processes. This is the reason that the conventional Johnson-Cook strength model does not adequately represent strain-hardening behavior of a material under high-temperature deformation conditions.

The strain-rate and the temperature terms in Eq 1 collectively account for the thermally activated nature of the plastic deformation process. It should be recognized that the effects represented by these two terms are of a reversible nature and they do not account for any permanent changes in the material microstructure (e.g., those brought about by the annealing and recrystallization processes) due to the exposure of the material to high temperatures. This is yet another reason that the original Johnson-Cook material model is not suitable for use in the computational analyses of hot-working processes.

### 1.2 AA5083-H131 Al-Mg-Mn Alloy (Ref 2)

Wrought aluminum alloys (AA) are divided into seven major classes according to their principle alloying elements. The Al-Mg AA5xxx alloys possess high *rollability*, they are readily available as plates and, due to their high corrosion resistance and relatively high strength and good welding quality, they are often used in various structural and armor applications. The non-age-hardenable AA5083 (nominal chemical composition: 4.5 wt.% Mg, 0.25 wt.% Cr, and 0.75 wt.% Mn) is an Mg/Mn solid-solution strengthened alloy and, in addition, in its H131 temper state is cold-work hardened and stabilized (to obtain a needed level of aging/over-aging resistance). While $Al_6Mn$ precipitates are present in this alloy, due to aforementioned stabilizing heat-treatment, they are relatively resistant to both dissolution and coarsening so that precipitate-portion of the material microstructure can be taken as mainly unchanged during FSW.

It should be also noted that AA5083 is often used in aerospace and in automotive industries for production of structural components with highly complex shapes. In these cases, the alloy is processed using super-plastic forming (a high-temperature, low-deformation-rate, low-forming-pressure, open/close-die forming process). After relatively severe cold-working treatment, the alloy is recrystallized. The presence of very-fine $Al_6Mn$ precipitates promotes/stimulates grain nucleation during the recrystallization process resulting in an ultra-fine grain-microstructure. Such microstructure enables plastic deformation by grain-boundary sliding (in addition to dislocation-based plasticity) and provides super-plastic behavior to the material when deformed under low-deformation-rate/high-temperature conditions. As will be shown below, since the material residing in the weld nugget FSW region is normally subjected to very high levels of plastic deformation and tends to recrystallize dynamically, one would expect formation of a very-fine grain-microstructure in this region. However, due to the attendant relatively high deformation rates, one does not generally expect significant contribution of grain-boundary sliding to the plastic deformation process.

### 1.3 Butt FSW

In contrast to the traditional fusion-welding technologies, FSW is a solid state metal-joining process which is generally employed in applications in which the original material microstructure/properties must remain unchanged as much as possible after joining (Ref 3-5). In this process, as shown in Fig. 1(a), a rotating tool moves along the contacting surfaces of two rigidly butt-clamped plates. As seen in this figure, the tool consists of a cylindrical pin which is threaded, at one end, and equipped with a shoulder, at the other. Also, during joining, the work-piece (i.e., the two clamped plates) is generally placed on a rigid backing support. At the same time, the shoulder is forced to make a firm contact with the top surface of the work-piece. As the tool (rotates and) moves along the butting surfaces, heat is being generated at the shoulder/work-piece and, to a lesser extent, at the pin/work-piece contact surfaces, as a result of the

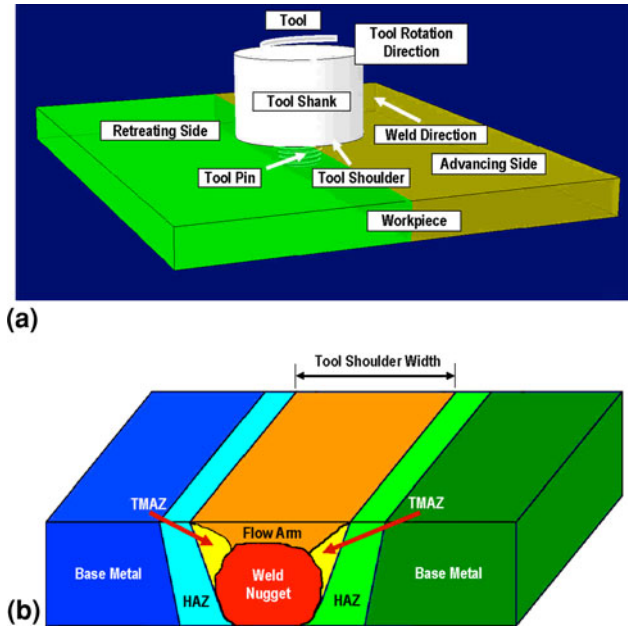


**Fig. 1** (a) A schematic of the FSW process; and (b) the main microstructural zones associated with the typical FSW joint

frictional-energy dissipation. This, in turn, causes an increase in temperature and gives rise to softening of the material adjacent to these contacting surfaces. As the tool advances along the butting surfaces, thermally softened material in front of the tool is (heavily) deformed, extruded around the tool to the region behind the tool and compacted/forged to form a joint/weld.

FSW has become the preferred technique for joining/welding *Difficult-to-weld* metals like AA, since its discovery in 1991 (Ref 3). Currently, shipbuilding, marine, aerospace, railway, and land transportation industries use FSW extensively as a joining process. Relative to the traditional fusion-welding technologies, FSW offers a number of advantages such as: (a) good mechanical properties in the *as-welded* condition; (b) improved safety due to the absence of toxic fumes or the spatter of molten material; (c) no consumables such as the filler metal or gas shield are required; (d) ease of process automation; (e) ability to operate in all positions, (horizontal, vertical, overhead, orbital, etc.), as there is no weld pool; (f) minimal thickness under/over-matching which reduces the need for expensive post-weld machining; and (g) low environmental impact. However, some disadvantages of the FSW process have also been identified such as: (a) an exit hole is left after the tool is withdrawn from the work-piece; (b) relatively large tool press-down and plate-clamping forces are required; (c) lower flexibility of the process with respect to variable-thickness and non-linear welds; and (d) often associated with lower welding rates than conventional fusion-welding techniques, although this shortcoming is somewhat lessened since fewer welding passes are required.

FSW normally involves complex interactions and competition between various mass and heat transport phenomena, plastic deformation and damage/fracture mechanisms, and microstructure-evolution processes (e.g., Ref 6, 7). Consequently, the material microstructure (and mechanical properties) in the weld region are highly complex and spatially diverse. Metallographic examinations of the FSW joints typically reveal the existence of the following four weld zones (not counting the unaffected/base-metal zone which is far enough from the weld so that material microstructure/properties are not altered by the joining process), Fig. 1(b): (a) the heat-affected zone (HAZ) in which material microstructure/properties are affected only by the thermal effects associated with FSW. While this zone is normally found in the case of fusion-welds, the nature of the microstructural changes (e.g., recovery, recrystallization, grain-growth, precipitate coarsening, precipitate dissolution, etc., depends on the work-piece material chemical composition and microstructural state) may be different in the FSW case due to generally lower temperatures and a more diffuse heat source; (b) the thermo-mechanically affected zone (TMAZ) is located closer than the HAZ to the work-piece components contact interface. Consequently, both the thermal and the mechanical aspects of the FSW process affect the material microstructure/properties in this zone. While the original grains are retained in this zone they experience a considerable amount of plastic deformation during the FSW process. Consequently, it is often observed (using metallographic analysis of the transverse and horizontal weld sections) that the grains have been subjected to bending; (c) the weld *nugget* is the innermost zone of an FSW joint. As a result of the way the material is transported from the regions ahead of the tool to the wake regions behind the tool, this zone typically contains the so-called onion-ring features. The material in this region has been subjected to the most severe conditions of plastic deformation and high-temperature exposure and consequently contains a very-fine dynamically recrystallized (equiaxed grain) weld microstructure. The width of the nugget is slightly larger than the FSW-tool pin diameter; and (d) the last FSW zone which is located above the weld nugget is generally referred to as the *flow-arm*. This weld zone typically contains the work-piece material which was (during welding) temporarily confined by the upright truncated-conical profile of the FSW-tool shoulder underside.

The FSW joint-quality is typically affected by the following welding/process parameters: (a) rotational and transverse velocities of the tool; (b) tool-plunge depth; (c) tool tilt-angle; and (d) tool-design/material. Since, in-general, higher temperatures are encountered in the case of higher rotational and lower transverse tool velocities, it is critical that a delicate balance between these two velocities is attained. Specifically, if the temperatures in the weld region are not high enough and the material has not been sufficiently softened, the weld zone may develop various flaws/defects arising from low ductility of the material. Conversely, when the temperatures are too high undesirable changes in the material microstructure/properties may take place and possibly incipient-melting flaws may be created during joining. To ensure that the necessary level of shoulder/work-piece contact pressure is attained and that the tool fully penetrates the weld, the tool-plunge depth (defined as the depth of the lowest point of the shoulder below the surface of the welded plate) has to be set correctly. Typically, insufficient tool-plunge depths result in low-quality welds (due to inadequate forging of the material at the rear of the tool), while excessive tool-plunge depths lead to under-matching of the weld thickness compared to the base-material thickness. Tool rearward tilting by 2°-4° has been often found to be beneficial since it enhances the effect of the forging process (Ref 8, 9).

FSW process has been investigated extensively using experimental means over the last two decades. The research carried out helped gain a better understanding of the FSW joining mechanisms and the accompanying evolution of the welded-material microstructure/properties (e.g., Ref 10, 11), as well as it helped rationalize the effect of various FSW process parameters on the weld quality/integrity (e.g., Ref 6, 12). It should be recognized, however, that the aforementioned experimental efforts were able to only correlate the *post-mortem* welded-materials microstructure/properties with the FSW process parameters and provided relatively little real-time insight into the physics of heat/mass transfer and microstructure-evolution processes. As shown in our previous study (Ref 13-20), this insight can be gained by carrying out a detailed physically based computational investigation of the FSW process. However, for this approach to be successful it was shown that physically based, high fidelity material models must be available for the work-piece material over a relatively large plastic strain, plastic strain-rate, and temperature ranges.

### 1.4 Objectives

The main objective of this study is to modify the original Johnson-Cook material model, as defined by Eq 1, to account for the aforementioned microstructural changes in the work-piece material during FSW. Towards that end, the following specific tasks had to be accomplished:

(a) Identification of the key microstructural parameters in AA5083-H131 which control the mechanical behavior of this material;

(b) Determination of the microstructure-evolution processes and the associated material-state-dependent evolutionary equations;
(c) Numerical integration of the evolutionary equations over an arbitrary material deformation history; and
(d) Appropriate modification of the original Johnson-Cook model to make the material model parameters dependent on the material microstructure parameters.

### 1.5 Organization

Details regarding the modifications of the original Johnson-Cook material-strength model are presented and discussed in section 2. The fully coupled thermo-mechanical analysis used in the computational investigation of the FSW process is presented in section 3. The main results obtained in this study are reported in section 4. The main conclusions resulting from the present study are summarized in section 5.

## 2. Johnson-Cook Model: Modification and Implementation

In this section, details are presented regarding the modifications make to the original Johnson-Cook strength model and of the steps taken to implement these modifications into a user subroutine which could be readily linked with a commercial finite-element program.

### 2.1 Modifications of the Johnson-Cook Model

As indicated in Eq 1, the Johnson-Cook constitutive model contains four terms: (a) the as-annealed material-strength, represented by parameter $A$; (b) the strain-hardening term; (c) the strain-rate dependency term; and (d) the reversible thermal-softening term. The Johnson-Cook material model modifications proposed in this study include only the first two terms since it was concluded that the strain-rate dependency and the reversible thermal-softening effects are, to a first order, correctly accounted for by the original Johnson-Cook model.

**2.1.1 Modifications in the Parameter *A*.** For solution strengthened (i.e., non-age hardened) alloys like AA5083, magnitude of the parameter $A$ is mainly affected by the material grain-size. To capture this effect, the Hall-Petch (grain-size dependency of the yield strength) equation in the form

$$A = A_{HP} + K_{HP} D^{-\frac{1}{2}} \qquad \text{(Eq 2)}$$

is adopted, where $A_{HP}$(=50 MPa) is the single crystal annealed yield strength, $K_{HP}$ is an alloy-specific, grain-size invariant parameter, and $D$ represents the mean grain-size.

For a given material in the as-received condition, $A$ and $D$ are known (or can be determined) then using Eq 2 one can evaluate parameter $K_{HP}$. Subsequently, as the material grain-size changes (due to the interplay of dynamic-recrystallization and grain-coarsening processes), one can calculate the associated value of parameter $A$ using Eq 2. When this procedure was applied to AA5083-H131 with an initial grain-size of 50 μm and the corresponding $A$ = 167 MPa, $K_{HP}$ = 827 MPa μm$^{1/2}$ is obtained. The corresponding grain-size dependence of the Johnson-Cook parameter $A$ is depicted in Fig. 2.

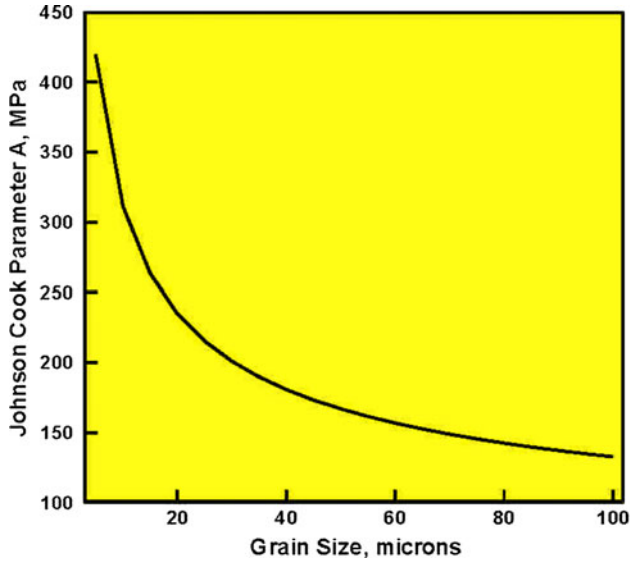


**Fig. 2** Grain-size dependence on the Johnson-Cook parameter $A$ in AA5083-H131

**2.1.2 Modifications in the Strain-Hardening Term.** As explained earlier, the strain-hardening term in Eq 1 uses equivalent plastic strain, $\bar{\varepsilon}^{pl}$, as a measure of the dislocation density within the material. The assumed correlation between the two quantities is generally valid as long as the extent of material annealing/recrystallization is relatively small. This condition, as discussed earlier, is not generally satisfied in the material residing within the weld region. To overcome this problem, a modified equivalent plastic strain measure, $\bar{\varepsilon}^{pl}_{mod}$, is introduced. The main difference between the two measures of the equivalent plastic strain is that $\bar{\varepsilon}^{pl}$ continuously increases with an increase in plastic deformation, while $\bar{\varepsilon}^{pl}_{mod}$ is allowed to decrease (as a consequence of the annealing/recrystallization processes). In other words, $\bar{\varepsilon}^{pl}$ is a measure of the extent of plastic deformation, while $\bar{\varepsilon}^{pl}_{mod}$ is the measure of the associated dislocation density.

**2.1.3 Grain-Size Evolution Equation.** Implementation of the proposed modifications to parameter $A$ suggested above require formulation of a grain-size evolution equation. In the incremental form, this equation can be written as:

$$D(t + \Delta t) = D(t) + \dot{D}_{\text{coarsening}} \Delta t + \dot{D}_{\text{refinement}} \Delta t \qquad \text{(Eq 3)}$$

where $\dot{D}_{\text{coarsening}}$ (a positive quantity) and $\dot{D}_{\text{refinement}}$ (a negative quantity) are, respectively, the rates of grain-size coarsening due to Oswald ripening and grain-size refinement due to dynamic-recrystallization.

According to Eq 3, grain-size evolution over any deformation history can be determined provided the two rate functions $\dot{D}_{\text{coarsening}}$ and $\dot{D}_{\text{refinement}}$ are known (i.e., the corresponding functional forms are established and the associated parameters determined). In the remainder of this section, simple expressions are introduced for the two grain-size rate functions and parameterized for the case of AA5083-H131.

The $\dot{D}_{\text{coarsening}}$ function reflects the rate of growth of material grains when the material is subjected to high temperatures. Under the most commonly used FSW process conditions, only the evidence for normal grain-growth was observed. In other words, grains in the HAZ, TMAZ, weld nugget, and flow-arm regions are found to grow in a continuous uniform manner and generally

no evidence is found of the so-called abnormal grain-growth (a process within which only few grains grow at the expense of the surrounding grains while the size of the (yet unconsumed) surrounding grains remains essentially unchanged).

Typically, the kinetics of normal grain-growth is defined by a function which relates the grain-size growth rate to the inverse of the grain-size as:

$$\dot{D}_{\text{coarsening}} = \frac{k_{\text{coarsening}}}{D} \quad \text{(Eq 4)}$$

where $k_{\text{coarsening}}$ is a temperature-dependent parameter. Integration of Eq 4 at a constant temperature yields:

$$D^2 - D_0^2 = 2k_{\text{coarsening}}t \quad \text{(Eq 5)}$$

Since the grain-growth process is of a thermally activated character, $k_{\text{coarsening}}$ is generally assumed to be given by an Arrhenius-type equation in the form:

$$k_{\text{coarsening}} = k_{\text{coarsening},0}e^{\frac{-Q_{\text{coarsening}}}{RT}} \quad \text{(Eq 6)}$$

where $k_{\text{coarsening},0}$ is the pre-exponential rate term (assumed constant for a given material), $Q_{\text{coarsening}}$ is the activation energy (also assumed to be constant for a given material), $R$ is the universal gas constant, and $T$ is the absolute temperature.

According to Eq 4, $\dot{D}_{\text{coarsening}}$ can be determined provided $k_{\text{coarsening},0}$ and $Q_{\text{coarsening}}$ parameters are known for a given system. To determine these parameters, isothermal grain-coarsening data at several temperatures reported in Ref 21 are used. These data are first used to compute an average value of $k_{\text{coarsening}}$ at a given temperature and then a linear-regression analysis was applied to the ln $(k_{\text{coarsening}})$ versus $-1/RT$ data to determine $k_{\text{coarsening},0}$ (equal to the exponent of the constant-term linear-regression coefficient) and $Q$ (equal to the linear term regression coefficient). This procedure yielded $k_{\text{coarsening},0}$(=31.59 $\mu m^2/s$) and $Q_{\text{coarsening}} = 23.75$ kJ/mol. The effect of iso-chronal high-temperature exposure for a 0.5-50.0 s time range (generally encountered in the FSW process) on the grain-size in AA5083-H131 with an initial grain-size of 50 μm is depicted in Fig. 3. It is seen that no excessive grain-growth is expected during FSW due to relatively short high-temperature exposure times. This finding is in good agreement with the general observations (e.g., Ref 17).

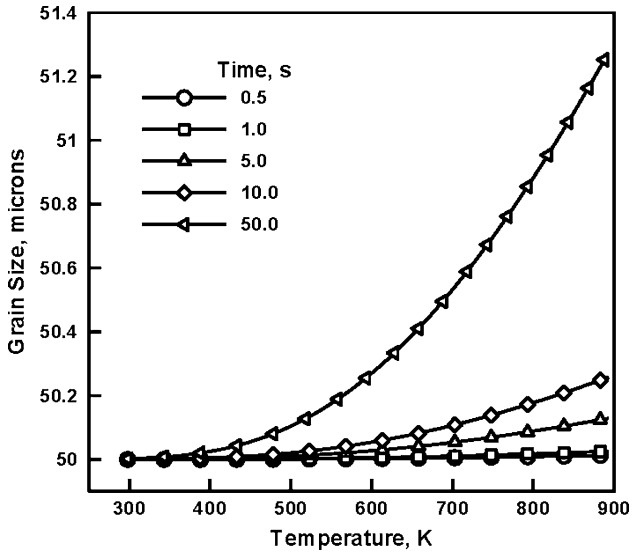


**Fig. 3** Effect of iso-chronal high-temperature exposure on the grain-size in AA5083-H131 with an initial grain-size of 50 μm

It should be noted that the assumption regarding constancy of grain-coarsening parameters, $k_{\text{coarsening},0}$ and $Q_{\text{coarsening}}$, used in Eq 5, are strictly valid only over a relatively narrow temperature and equivalent plastic strain range. Nevertheless, even if this assumption is not employed, one should not expect significant grain-growth to take place during the FSW process.

As far as the grain refinement rate parameter is concerned, following the analysis presented in our recent study (e.g., Ref 14-18), it is assumed to scale with an increment of the recrystallization-corrected equivalent plastic strain $\Delta\bar{\varepsilon}^{\text{pl}}_{\text{recrystallized}}$ (defined below) as:

$$\dot{D}_{\text{refinement}} = D_{\text{refinement}}\frac{\Delta\bar{\varepsilon}^{\text{pl}}_{\text{recrystallized}}}{\Delta t} \quad \text{(Eq 7)}$$

Following the procedure for the assessment of $\Delta\bar{\varepsilon}^{\text{pl}}_{\text{recrystallized}}$ (given below) and the experimental grain-size results reported in Ref 22, parameter $D_{\text{refinement}}$ has been evaluated as 17 μm.

**2.1.4 Evolution of the Recrystallization-Modified Equivalent Plastic Strain.** Implementation of the proposed modifications to strain-hardening term suggested above requires formulation of a recrystallization-modified equivalent plastic strain evolution equation. In the incremental form, this equation can be written as:

$$\bar{\varepsilon}^{\text{pl}}_{\text{mod}}(t+\Delta t) = \bar{\varepsilon}^{\text{pl}}(t) + \Delta\bar{\varepsilon}^{\text{pl}} + \Delta\bar{\varepsilon}^{\text{pl}}_{\text{recrystallized}} \quad \text{(Eq 8)}$$

where $\Delta\bar{\varepsilon}^{\text{pl}}$ (a positive quantity) is an increase in the equivalent plastic strain due to continuation of plastic deformation and $\Delta\bar{\varepsilon}^{\text{pl}}_{\text{recrystallized}}$ (a negative quantity) reflects a decrease in the equivalent plastic strain which reflects a decrease in dislocation density during a time increment $\Delta t$ due to the effect of dynamic-recrystallization. $\Delta\bar{\varepsilon}^{\text{pl}}$ is directly computed by ABAQUS/Explicit, while following the procedure proposed in our recent study (Ref 13-17), $\Delta\bar{\varepsilon}^{\text{pl}}_{\text{recrystallized}}$ is defined within this study as:

$$\Delta\bar{\varepsilon}^{\text{pl}}_{\text{recrystallized}} = \left(\dot{\bar{\varepsilon}}^{\text{pl}}_{\text{recrystallized}}\left(\bar{\varepsilon}^{\text{pl}}_{\text{recrystallized}}\right)^{p} e^{\frac{-Q_{\text{recrystallized}}}{RT}}\right)\Delta t \quad \text{(Eq 9)}$$

where $\dot{\bar{\varepsilon}}^{\text{pl}}_{\text{recrystallized}}$ and $p$ are a pre-exponential (negative) rate and a (positive) power term, respectively, and $Q_{\text{recrystallized}}$ is the associated recrystallization energy. It should be noted that $\bar{\varepsilon}^{\text{pl}}_{\text{recrystallized}}$ term ensures that no recrystallization takes place in a fully annealed material.

By carrying out a separate finite-element analysis of the so-called equal channel angular pressing process, post-processing the data using an inverse engineering analysis and comparing the results with the experimental ones reported in Ref 22, the following values were obtained: $\dot{\bar{\varepsilon}}^{\text{pl}}_{\text{recrystallized}} = -0.15/s$, $p = 2.7$, and $Q_{\text{recrystallized}} = 21.5$ kJ/mol. Details regarding this portion of the study will be presented in a future communication. An example of the results obtained in this portion of the study is displayed in Fig. 4 in which $\bar{\varepsilon}^{\text{pl}}_{\text{recrystallized}}$ is plotted as a function of time at several temperatures and under a constant uniaxial plastic strain-rate of 0.1/s. It is seen that, at low temperatures (e.g., 400 K), plastic deformation dominates material response and, consequently, $\bar{\varepsilon}^{\text{pl}}_{\text{recrystallized}}$ continues to increase with the extent of plastic deformation. In fact, the

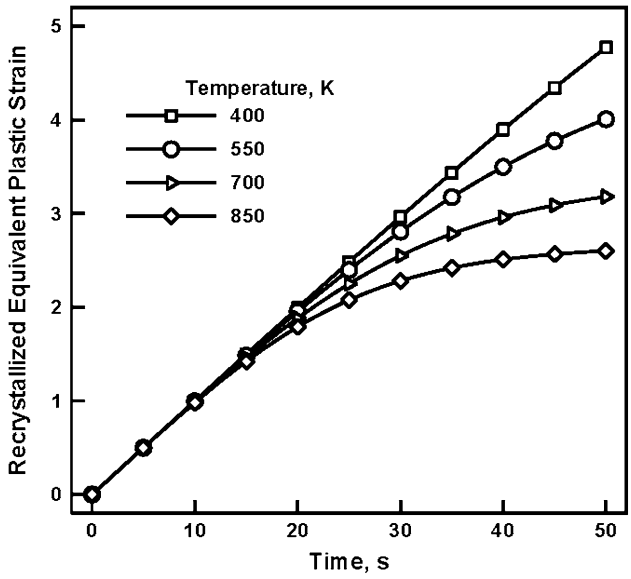


**Fig. 4** The effect of high-temperature exposure time on the isothermal recrystallized equivalent plastic strain in AA5083-H131 deformed at a uniaxial plastic strain-rate of 0.1/s

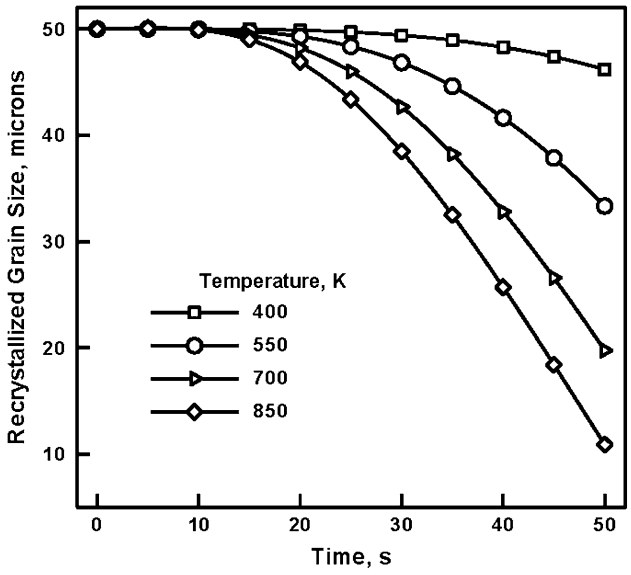


**Fig. 5** The effect of high-temperature exposure time on the isothermal recrystallized grain-size in AA5083-H131 deformed at a uniaxial plastic strain-rate of 0.1/s

magnitude of $\bar{\varepsilon}^{pl}_{recrystallized}$ is effectively identical to that of $\bar{\varepsilon}^{pl}$ in this temperature range. In sharp contrast, at higher temperatures (e.g., 850 K), an equilibrium is reached between the plastic deformation and dynamic-recrystallization processes resulting in a temperature-dependent steady state value of $\bar{\varepsilon}^{pl}_{recrystallized}$. It is also seen that the steady state value of $\bar{\varepsilon}^{pl}_{recrystallized}$ decreases with an increase in temperature confirming that, at higher temperatures, the extent of recrystallization is greater and results in a smaller value of the dislocation density.

The associated changes in the material grain-size are depicted in Fig. 5. It is seen that in the presence of considerable amount of plastic deformation and high temperatures, due to a high rate of dynamic-recrystallization a considerable reduction in material grain-size can ensue.

### 2.2 Implementation of the Johnson-Cook Model

Since all the calculations carried out in this study have been done using ABAQUS/Explicit commercial finite-element software (Ref 23), the modified Johnson-Cook model is implemented in this program. In our prior study (Ref 13-17), modifications in the material model were implemented using a user material subroutine VUMAT. However, since ABAQUS/Explicit already has the original Johnson-Cook material model implemented, it was decided that an advantage be taken of this implementation. Consequently, the so-called VUSDFLD user subroutine was used which enables introduction of the new material-state-dependent variables (i.e., variables which quantify the current microstructural state of the material) and new field variables (i.e., variables which directly/explicitly affect the material mechanical response). Consequently, implementation of the modified Johnson-Cook material model included the following two steps:

(a) The analytical form of the Johnson-Cook model involving specification of the material model parameters ($A$, $B$, $n$, …) is replaced with a piecewise-linear definition of the same model. Within the latter material model definition, the effect of the equivalent plastic strain as computed by ABAQUS is excluded and is replaced with its user-defined analog, $\bar{\varepsilon}^{pl}_{recrystallized}$ (the first field variable) which accounts for the annealing/recrystallization effects (as discussed above). In addition, material yield strength is made dependent on temperature (in accordance with original Johnson-Cook model) and on the grain-size (the second field variable). Following the ABAQUS/Explicit syntax, an analytical representation of the strain-rate effect is retained. Thus, within the piecewise portion of the modified Johnson-Cook material model, material-strength depends on three variables, i.e., temperature and the two field variables. To represent the modified Johnson-Cook material model in a piecewise-linear fashion, the three-dimensional temperature versus field variable 1 versus field variable 2 domain is discretized using a regular mesh and the yield strength magnitude is defined at each nodal point. Thus, for any combination of the temperature and the two field variables, material-strength (at the reference strain-rate) can be determined via linear interpolation. Then the effect of the non-reference strain-rate is included using the term within the second pair of parenthesis in Eq 1; and

(b) An appropriate VUSDFLD user subroutine is then developed within which the two field variables are continuously updated and returned to the ABAQUS solver for use. In addition, within the same subroutine three state variables are also defined: (a) the equivalent plastic strain which includes the effect of annealing/recrystallization; (b) the material grain-size; and (c) the increment in the equivalent plastic strain as computed by ABAQUS. These state variables are used to update the field variables, in a procedure which requires the knowledge of the two field variables and the equivalent plastic strain at the end of the previous time increment. However, ABAQUS explicit does not provide for saving and the retrieval of the field variables from one time increment to another.

## 3. Computational Analysis of the FSW Process

Modeling of the FSW process carried out in this study employed the fully coupled thermo-mechanical finite-element procedure developed in out prior study (Ref 13-17). Since a detailed account of the procedure was provided in Ref 13-17, only a brief overview of it will be presented in the remainder of this section.

### 3.1 Computational Domain and Meshed Models

The computational domain used consists of a (40.0 mm radius, 3.0 mm thickness) circular plate/work-piece (with a concentric through-the-thickness 3.0 mm radius circular hole) and a two-part tool (consisting of a 3.0 mm radius, 3.0 mm length solid right circular cylinder, at the bottom, and a 9.0 mm radius, 3.0 mm thickness circular-plate section, on the top), Fig. 6(a), (b).

The work-piece and the FSW-tool geometrical models described above are meshed using ~15,000 first-order eight-node reduced-integration hexahedral thermo-mechanically coupled solid elements. A close-up of the meshed model used in this study is depicted in Fig. 7.

### 3.2 Computational Procedure

**3.2.1 Computational Algorithm.** The FSW process is analyzed computationally using a fully (two-way) coupled thermo-mechanical finite-element algorithm within which heat dissipation associated with plastic deformation and tool/work-piece interfacial friction-sliding is treated as a source in the governing heat conduction equation(s) while the effect of temperature on the mechanical response of the work-piece material is taken into account through the use of a temperature-dependent work-piece material model. As established earlier, work-piece material in the nugget and TMAZ regions experience large plastic deformations during FSW. Under these circumstances, the use of a Lagrangian approach in which the finite-element mesh is attached to and moves with the material may display serious numerical problems (due to excessive mesh distortion). To overcome this problem, an ALE formulation is used within which adaptive re-meshing is carried out to maintain good quality mesh. The fully coupled thermo-mechanical problem dealing with FSW is solved using an explicit solution algorithm implemented in ABAQUS/Explicit (Ref 23), a general purpose finite-element solver.

**3.2.2 Heat Sources.** As mentioned earlier, both plastic deformation and frictional sliding are treated as heat sources. To account for the fact that a small fraction of the plastic-deformation work is stored in the form of crystal defects, 95% of this study was assumed (arbitrarily) to be dissipated in the form of heat. As far as heat generation due to frictional sliding is concerned, it is assumed that its rate scales with the product of local interfacial shear stress and the sliding rate, and that 100% of this energy is dissipated in the form of heat.

**3.2.3 Initial and Boundary Conditions.** The analysis is carried out by prescribing from the onset a constant rotational velocity and a constant downward pressure to the tool. Instead of assigning a travel velocity to the tool along the (postulated) butting surfaces of the work-piece, the work-piece material is forced to move through the work-piece computational domain at the same velocity but in the opposite direction. This was accomplished by prescribing from the onset of the FSW simulation a constant in-flow work-piece material velocity in a direction opposite to that of tool travel. Due to the use of this approach, it should be noted that, the circular plate displayed in Fig. 6(b) represents not the entire work-piece but rather a circular region around the tool in the otherwise infinitely long work-piece.

Additional boundary conditions employed are as follows:

(a) zero normal-velocity conditions applied over the bottom face of the work-piece to mimic the restraining effect of the work-piece rigid backing plate;
(b) the standard convective boundary conditions are applied over free surfaces of the work-piece and the tool; and
(c) enhanced convection boundary conditions are applied over the bottom face of the work-piece (to mimic the effect of enhanced heat extraction through the work-piece backing plate).

**3.2.4 Contact Interactions.** Work-piece/tool interactions are accounted for through the use of a penalty algorithm within which the extent of contact pressure is governed by the local surface penetrations while shear stresses are transferred via a "*slip/stick*" algorithm, i.e., shear stresses lower than the

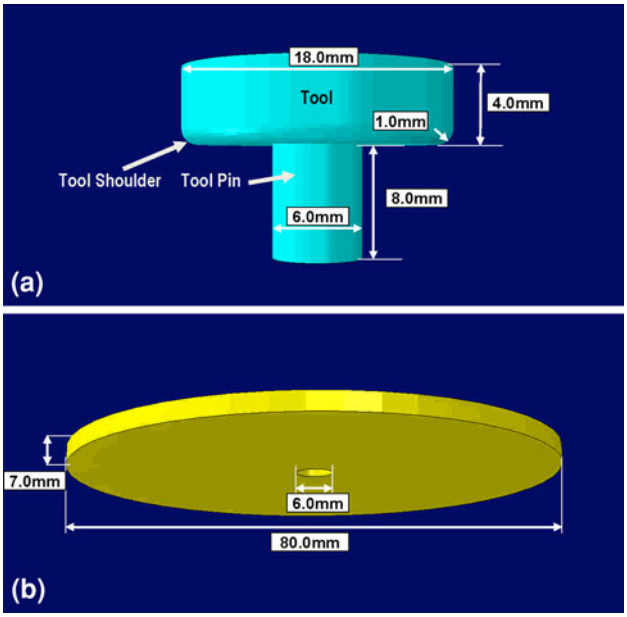


**Fig. 6** Geometrical models with dimensions for the (a) FSW tool and (b) FSW work-piece

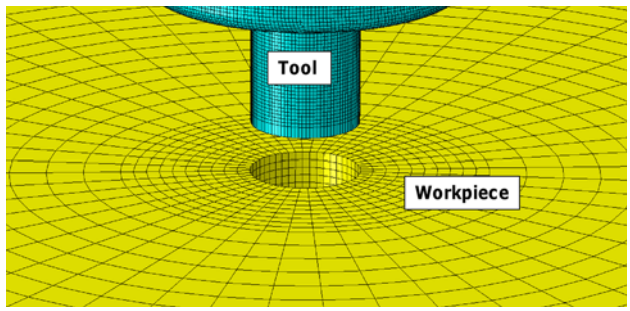


**Fig. 7** Meshed models for the tool and the work-piece used in this study

frictional shear stress are transferred without interface sliding (otherwise interface sliding takes place). The frictional shear stress is defined by a modified Coulomb law within which there is an upper limit to this quantity (set equal to the shear strength of the work-piece material). The frictional shear stress is then defined as a smaller of the product between the static/kinetic friction coefficient and the contact pressure, on one hand, and the work-piece material shear strength, on the other. Partitioning of the heat generated as a result of frictional sliding at the tool/work-piece contact interfaces is then computed using the appropriate thermal properties of the two materials (Ref 24).

**3.2.5 Mesh Sensitivity.** In order to ensure that the key results and conclusions yielded by this study are not affected by the choice of the computational mesh, a mesh sensitivity analysis was carried out involving the use of progressively fine finite-element meshes. The finite-element mesh finally selected is a compromise between the computational efficiency and the numerical accuracy.

**3.2.6 Computational Cost.** To keep the computational cost reasonable while ensuring stability and robustness of the computational procedure, a mass scaling algorithm is used. This algorithm adaptively adjusts material density in the critical finite elements without significantly affecting accuracy of the computational results. A typical 30 s FSW computational analysis required 10 h of (wall-clock) time on a 12 core, 3.0 GHz machine with 16 GB of memory.

### 3.3 Material Models

Since the tool normally experiences relatively lower deformation during FSW, it is modeled using a rigid-material formulation. Its density and (temperature dependent) thermal/thermo-mechanical properties are next set to that of AISI-H13, a hot-worked tool steel, frequently used as the FSW-tool material (Ref 16).

The work-piece material is assumed to be isotropic, linear-elastic and strain-hardenable, strain-rate sensitive, thermally softenable plastic material, and is modeled using the modified Johnson-Cook material model presented in section 2. Standard density and (temperature dependent) thermal properties of AA5083-H131 are used to define the thermal-portion of the material model.

### 3.4 Typical Results

In this section, a few typical FSW process simulation results pertaining to the spatial distribution and temporal evolution of a number of material-state variables (other than those describing material microstructure, e.g., grain-size) are presented and briefly discussed. Spatial distribution and temporal evolution of the variables describing material microstructure and of the affected mechanical properties will be presented in the next section.

**3.4.1 Equivalent Plastic Strain Field.** An example of the typical results pertaining to spatial distribution and temporal evolution of the equivalent plastic strain in the AA5083-H131 work-piece during FSW is displayed in Fig. 8(a), (b). It should be noted that the quantity displayed in these figures is the total equivalent plastic strain which quantifies the overall extent of plastic deformation experienced locally by the work-piece material and not its counterpart introduced in section 2, which scales with the dislocation density. Examination of the results displayed in these figures and of the results obtained in this study (but not shown for brevity) reveals that:

(a) In general, plastic strains in the 20 and 50 range are observed with the strain magnitude being controlled by FSW process conditions such as tool contact pressure, tool rotational, and translational speeds;
(b) The highest equivalent plastic strains are always found in the work-piece material right below the tool shoulder and equivalent plastic strains progressively decreased from this region as a function of the distance in the radial and through-the-thickness directions;
(c) Distribution of the equivalent plastic strains is highly asymmetric. This asymmetry is related to the differences in the material transport (at the advancing and the retreating sides of the weld) from the region ahead of the tool to the region behind the tool; and
(d) In general, equivalent plastic strain differences between the top and the bottom surfaces of the work-piece are reduced while equivalent plastic strain magnitudes are increased as the tool translational speed is decreased and the tool/work-piece contact pressure is increased. This finding suggests that under these FSW process conditions the extent of material stirring/mixing (which plays a critical role in weld quality/joint-strength) is increased.

**3.4.2 Nodal Velocity Field.** The distribution of nodal velocities at the outer surfaces of the work-piece at two different times (0.0 and 0.5 s) is displayed in Fig. 8(c), (d). For clarity, the tool is not shown. These figures clearly show that the initially assigned unidirectional velocity field in the direction of welding, quickly transforms into the velocity field in which there is a well-defined stir region right below the shoulder (within which the material circles around the pin) and the remainder of the field (within which the material tends to flow around the stir region). A comparison of the results displayed in Fig. 8(c), (d) clearly shows how the region underneath the tool shoulder which is initially unfilled becomes filled as FSW proceeds. Once the space under the shoulder is fully filled it remains filled as the FSW process continues. The material in this region is constantly being refreshed as the tool advances in the welding direction.

**3.4.3 Material/Tracer-Particle Trajectories.** It should be noted that the results displayed in Fig. 8(c) and (d) shows the spatial distribution and temporal evolution of the nodal velocities, respectively. Due to the arbitrary Lagrangian-Eulerian (ALE) character of the finite-element analysis used in this study, the motion of the finite-element mesh is not completely tied to the motion of the material. Consequently, the results displayed in Fig. 8(c), (d) shows the velocities of the material particles which at that moment pass through the nodal points in question. However, one must recognize that at different times different material particles are associated with the same nodes. In order to observe stirring of the material under the tool shoulder, one should monitor material-particle trajectories rather than nodal velocities. This is possible within ABAQUS/Explicit through the use of so-called tracer particles which are attached to the material points (and not to the mesh nodal points).

Figure 8(e) and (f) displays typical results pertaining to the trajectory of retreating-side and advancing-side tracer particles, respectively. The tracer particles displayed in these figures are initially located in a plane which is halfway between the top and bottom surfaces of the work-piece. For improved clarity, tracer-particle trajectories are color coded. The results displayed

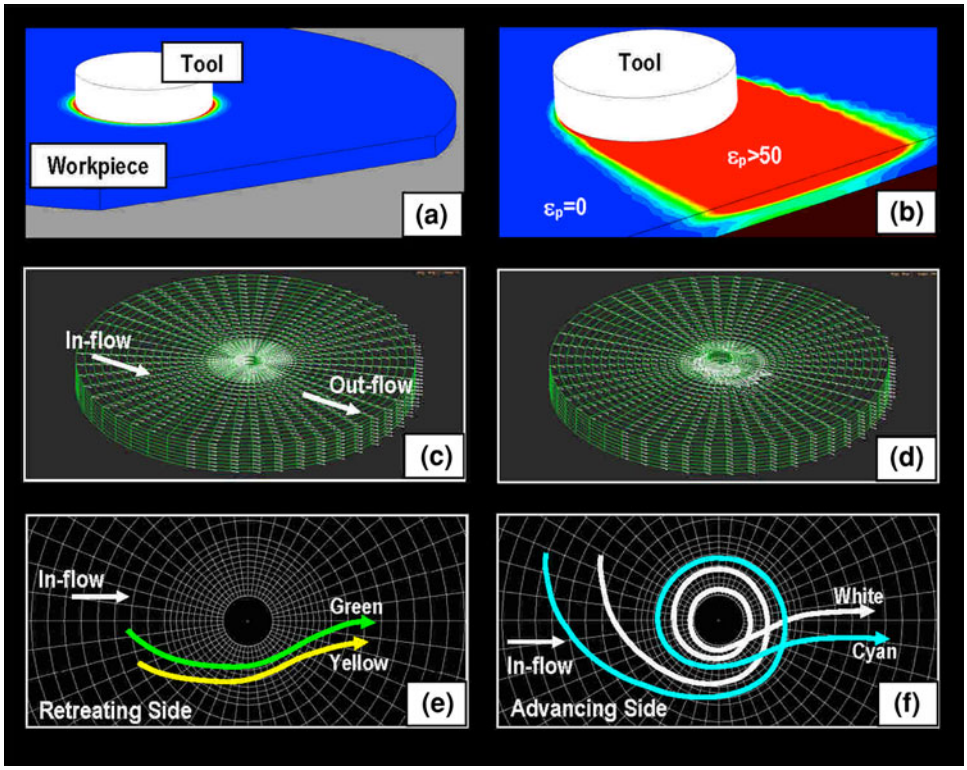


**Fig. 8** Typical FSW computational-analysis results pertaining to the steady state distribution of (a), (b) equivalent plastic strain; (c), (d) nodal velocities; (e) and (f) retreating-side and advancing-side tracer-particle trajectories, respectively

in Fig. 8(e), (f) clearly revealed the following basic aspects of the FSW process:

(a) At the retreating-side, work-piece material particles (as represented by the yellow and green tracer-particle trajectories, Fig. 8e) typically do not enter the stir zone under the tool-shoulder and usually only flow around it;
(b) At the advancing-side, work-piece material particles which are initially closer to the butting surfaces (as represented by the white and cyan tracer-particle trajectories, Fig. 8f), tend to pass over to the retreating-side and become co-stirred with some of the retreating-side material particles to form the welded joint; and
(c) At the advancing-side, work-piece material particles further away from the initial butting surfaces remain on the advancing-side and either enter the stir region on the advancing-side or flow around it.

**3.4.4 Temperature Field.** A typical spatial distribution of temperature in the work-piece during FSW is displayed in Fig. 9(a), (b). The results displayed in Fig. 9(a) and (b) refer to the temperature distributions over the medial longitudinal and medial transverse sections, respectively. Simple examination of the results displayed in these figures and of the results obtained in this study (but not shown for brevity) reveals that:

(a) Depending on the FSW process conditions such as tool contact pressure, tool rotational, and translational speeds, maximum temperatures in a range between 750 and 850 K are obtained;
(b) The highest temperatures are always found in the work-piece material right below the tool shoulder and temperatures are progressively decreased from this region as a function of the distance in the radial and through-the-thickness directions;
(c) As the tool rotational speed and contact pressure are increased, higher temperatures are observed and temperature differences between the top and the bottom surfaces of the work-piece are reduced; and
(d) Typically plastic deformation contributes around 30% to the overall heat generation (the remainder is associated with the frictional dissipation at the tool/work-piece contact surfaces) and this contribution increases slowly with an increase in the translational velocity of the tool.

## 4. Microstructure and Property Predictions

As discussed earlier, the modified Johnson-Cook material model introduced in section 2 and the FSW computational procedure overviewed in section 3 enable the prediction of the spatial distribution of material microstructure and properties within the weld. To demonstrate these aspects of the current approach, spatial distribution of the material grain-size and material room-temperature yield strength are computed and analyzed in this section.

### *4.1 Grain-Size Distribution Within the Weld*

An example of the average grain-size distribution over a transverse cut of the weld is shown in Fig. 10. It should be noted that the base-material initial grain-size was 50 μm. Careful examination of the results shown in Fig. 10 reveals the presence of a region with a slightly increased grain-size and another region with a considerably reduced grain-size. Based

solely on this finding, the first region can be assumed to comprise the HAZ and the TMAZ, while the second region includes the weld nugget and the flow-arm.

It should be noted at this point that: (a) the extents of the two regions as well as the grain-size spatial distribution within each are affected by the selection of the FSW process parameters (e.g., tool rotational and travel speeds, tool geometry, tool-plunge depth, etc.); and (b) the grain-size distribution within the weld greatly affects the mechanical properties (including blast survivability) of the weld. Thus the present approach can greatly contribute to the establishment of the basic processing/microstructure/property relations in the FSW joints.

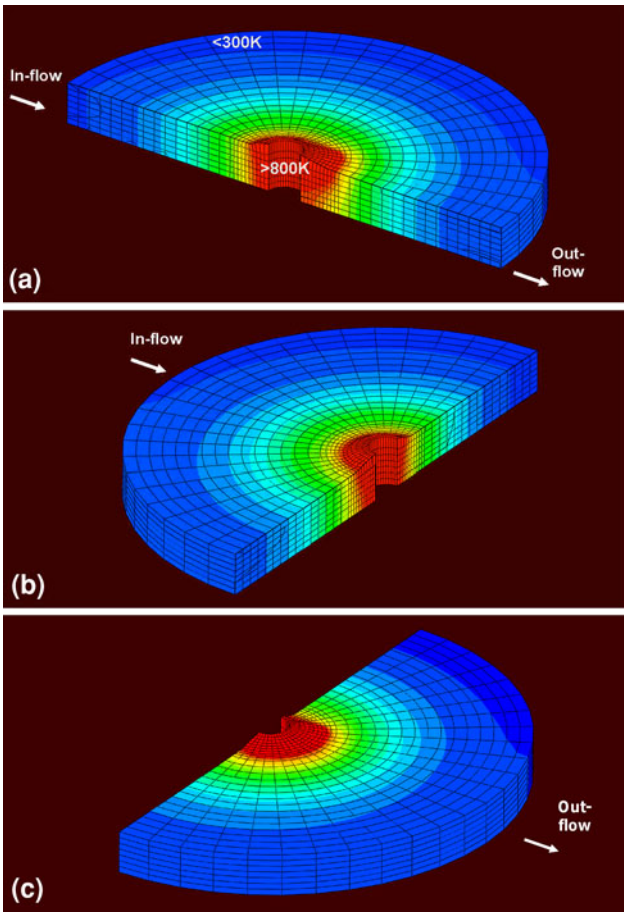


**Fig. 9** Typical temperature distribution over one-half of the work-piece obtained by cutting along: (a) the longitudinal; and (b), (c) transverse directions

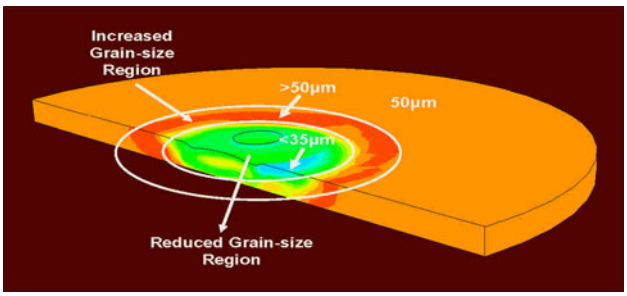


**Fig. 10** An example of the spatial distribution of grain-size across a transverse section of a FSW joint in AA5083-H131. Material initial grain-size of 50 μm

### 4.2 Room-Temperature Material Yield-Strength Distribution Within the Weld

An example of the room-temperature material yield-strength distribution over a transverse cut of the weld is shown in Fig. 11. It should be noted that the base-material initial yield-strength was 167 MPa. Careful examination of the results shown in Fig. 11 reveals three weld regions (not counting the base-metal):

(a) The inner-most region has an intermediate yield-strength value and is clearly associated with the weld nugget and flow-arm weld zones. The values of the material yield strength found in this region are clearly the result of the competition of two effects: (i) dynamic-recrystallization which appears to have not entirely removed the effects of strain-hardening present in the base-metal and acquired during FSW; and (ii) yield-strength increase associated with grain-size refinement observed in this region which appears to be potent enough to help overcome strength loss due to the removal of the cold-worked high dislocation density material microstructure;

(b) The inner, higher-strength region which corresponds to the TMAZ. In this region, deformation-induced strain-hardening overpowers dynamic-recrystallization-induced material softening giving rise to a net increase in the material-strength; and

(c) The region adjacent to the base-metal in which very small reductions in the material-strength are observed. This region clearly corresponds to the HAZ in which no plastic deformation takes place during FSW while the material is subject to slightly elevated temperatures.

As mentioned above, the extents of these different regions and the spatial distribution of the associated material parameter (yield-strength, in the present case) is affected by the selection of the FSW process parameters which enables establishment of the functional relationships between the FSW process and the resulting weld properties/performance.

## 5. Summary and Conclusions

Based on the study presented and discussed, the following main summary remarks and conclusions can be made:

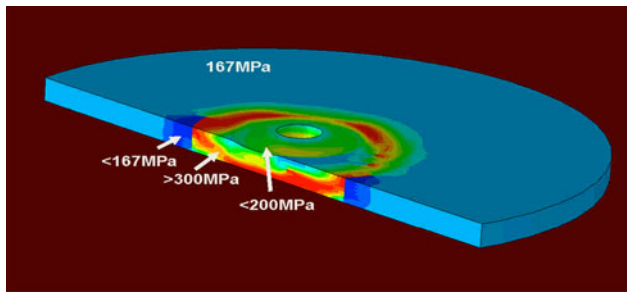


**Fig. 11** An example of the spatial distribution of room-temperature material yield strength across a transverse section of a FSW joint in AA5083-H131. Material initial yield strength is 167 MPa

1. Key shortcomings in the Johnson-Cook material model when used in the analysis of the FSW process are identified and the potential modifications in this model, which include the effects of grain-size and dynamic-recrystallization, proposed.
2. To demonstrate the utility of the modified Johnson-Cook material model, a series of finite-element analyses of the FSW of AA5083-H131 (a solid-solution strengthened and strain-hardened/stabilized Al-Mg-Mn alloy) is carried out.
3. The results obtained are used to predict the microstructure (as represented by the grain-size) and mechanical properties (e.g., room-temperature yield-strength) in different FSW zones.
4. Finally, it is discussed how the use of the modified Johnson-Cook work-piece material model and the FSW computational analysis can be used to establish processing/microstructure/property relations in the weld and, in turn, guide the selection of the welding-process parameters for optimum weld performance.

## Acknowledgments

The material presented in this paper is based on work supported by two Army Research Office sponsored grants (W911NF-11-1-0207 and W911NF-09-1-0513) and two U.S. Army/Clemson University Cooperative Agreements (W911NF-04-2-0024 and W911NF-06-2-0042).

## References

1. G.R. Johnson, W.H. Cook, A Constitutive Model and Data for Metals Subjected to Large Strains, High Strain Rates and High Temperatures, *Proceedings of the 7th International Symposium on Ballistics*, 1983
2. "Armor Plate, Aluminum Alloy, Weldable 5083 and 5456"; MIL-DTL-46027J, U.S. Department of Defense, Washington DC, August 1992
3. W.M. Thomas, E.D. Nicholas, J.C. Needham, M.G. Murch, P. Temple-Smith, and C. J. Dawes. Friction Stir Butt Welding, International Patent Application No. PCT/GB92/02203, 1991
4. C.J. Dawes and W.M. Thomas, Friction Stir Process Welds Aluminum Alloys, *Weld. J.*, 1996, **75**, p 41–52
5. W.M. Thomas and R.E. Dolby. Friction Stir Welding Developments, *Proceedings of the Sixth International Trends in Welding Research*, S. A. David, T. DebRoy, J. C. Lippold, H. B. Smartt and J. M. Vitek, Eds., ASM International, Materials Park, OH, USA, 2003, p 203–211
6. J.Q. Su, T.W. Nelson, R. Mishra, and M. Mahoney, Microstructural Investigation of Friction Stir Welded 7050-T651 Aluminum, *Acta Mater.*, 2003, **51**, p 713–729
7. W.B. Lee, C.Y. Lee, W.S. Chang, Y.M. Yeon, and S.B. Jung, Microstructural Investigation of Friction Stir Welded Pure Titanium, *Mater. Lett.*, 2005, **59**, p 3315–3318
8. H. Schmidt, T.L. Dickerson, and J. Hattel, Material Flow in Butt Friction Stir Welds in AA2024-T3, *Acta Mater.*, 2006, **54**, p 1199–1209
9. L. Fratini, G. Buffa, D. Palmeri, J. Hua, and R. Shivpuri, Material Flow in FSW of AA7075–T6 Butt Joints: Numerical Simulations and Experimental Verifications, *Sci. Technol. Weld. Join.*, 2006, **11**, p 412–421
10. R.S. Mishra and Z.Y. Ma, Friction Stir Welding and Processing, *Mater. Sci. Eng. R*, 2005, **50**, p 1–78
11. H.W. Zhang, Z. Zhang, and J.T. Chen, The Finite Element Simulation of the Friction Stir Welding Process, *Mater. Sci. Eng. A*, 2005, **403**, p 340–348
12. H.G. Salem, A.P. Reynolds, and J.S. Lyons, Microstructure and Retention of Superplasticity of Friction Stir Welded Superplastic 2095 Sheet, *Scripta Mater.*, 2002, **46**, p 337–342
13. M. Grujicic, G. Arakere, H.V. Yalavarthy, T. He, C.-F. Yen, and B.A. Cheeseman, Modeling of AA5083 Material-microstructure Evolution During Butt Friction-Stir Welding, *J. Mater. Eng. Perform.*, 2010, **19**(5), p 672–684
14. M. Grujicic, G. Arakere, C.-F. Yen, and B.A. Cheeseman, Computational Investigation of Hardness Evolution During Friction-stir Welding of AA5083 and AA2139 Aluminum Alloys, *J. Mater. Eng. Perform.*, 2010, **20**(7), p 1097–1108
15. M. Grujicic, G. Arakere, B. Pandurangan, A. Hariharan, C.-F. Yen, B.A. Cheeseman, and C. Fountzoulas, Statistical Analysis of High-Cycle Fatigue Behavior of Friction Stir Welded AA5083–H321, *J. Mater. Eng. Perform.*, 2010, **20**(6), p 855–864
16. M. Grujicic, T. He, G. Arakere, H.V. Yalavarthy, C.-F. Yen, and B.A. Cheeseman, Fully-Coupled Thermo-Mechanical Finite-Element Investigation of Material Evolution During Friction-Stir Welding of AA5083, *J. Eng. Manuf.*, 2010, **224**(4), p 609–625
17. M. Grujicic, G. Arakere, B. Pandurangan, A. Hariharan, C.-F. Yen, and B.A. Cheeseman, Development of a Robust and Cost-effective Friction Stir Welding Process for use in Advanced Military Vehicle Structures, *J. Mater. Eng. Perform.*, 2011, **20**(1), p 11–23
18. M. Grujicic, G. Arakere, B. Pandurangan, A. Hariharan, C.-F. Yen, B.A. Cheeseman, and C. Fountzoulas, Computational Analysis and Experimental Validation of the Ti-6Al-4V Friction Stir Welding Behavior, *J. Eng. Manuf.*, 2011, **225**(2), p 208–223
19. M. Grujicic, G. Arakere, A. Hariharan, B. Pandurangan, C-.F. Yen, and B.A. Cheeseman, A Concurrent Design, Manufacturing and Testing Product Development Approach for Friction-stir Welded Vehicle Underbody Structures, J. Mater. Eng. Perform. 2010. doi: 10.1007/s11665-011-9955-7
20. M. Grujicic, G. Arakere, B. Pandurangan, A. Hariharan, C.-F. Yen, B.A. Cheeseman, and C. Fountzoulas, Computational Analysis and Experimental Validation of the Ti-6Al-4V Friction Stir Welding Behavior, *J. Eng. Manuf.*, 2010, **224**(8), p 1–16
21. Z. Huda and T. Zaharinie, Kinetics of Grain Growth in 2024-T3: An Aerospace Aluminum Alloy, *J. Alloys Compd.*, 2009, **478**, p 128–132
22. I. Mazuruna, T. Sakai, H. Miura, O. Sitdikov, and R. Kaibishev, Effect of Deformation Temperature on Microstructure Evolution in Aluminum Alloy 2219 During Hot ECAP, *Mater. Sci. Eng. A*, 2008, **486**, p 662–671
23. ABAQUS Version 6.10EF, User Documentation, Dassault Systems, 2011
24. S. Xu, X. Deng, A.P. Reynolds, and T.U. Seidel, Finite Element Simulation of Material Flow in Friction Stir Welding, *Sci. Technol. Weld Join.*, 2001, **6**, p 191–193